A Deep Learning Strategy for Multipath Ghosts Filtering via Microwave Tomography

Giuseppe Esposito, Ilaria Catapano, *Member, IEEE*, Giovanni Ludeno, Francesco Soldovieri, and Gianluca Gennarelli

***Abstract*— Radar imaging algorithms generally exploit linear models of the electromagnetic scattering phenomenon. This assumption leads to qualitative and computationally effective data inversion schemes, which only account for direct scattering from targets, whereas multipath signal contributions are neglected. As a result, multipath ghosts, i.e., false targets reconstructed at positions where no real target exists, affect the radar images, thus preventing a reliable interpretation of the observed scene. This article proposes a fully data-driven deep learning (DL) approach based on a convolutional neural network (CNN) and microwave tomography to face this challenge. The approach achieves multipath ghost suppression for the case of small targets in terms of probing wavelength. In the proposed training scheme, the tomographic image affected by ghosts represents the input of the network while a ghost-free reconstruction is the output. Numerical simulations addressing the detection of metallic rebars via ground penetrating radar (GPR) are presented. As shown, the proposed ghost removal strategy is effective and robust to variations of the scenario parameters on which the network is trained. Finally, an experimental validation shows the effectiveness of the proposed strategy even in operative conditions.**

***Index Terms*— Convolutional neural network (CNN), inverse scattering problems, microwave tomography, multipath ghosts, radar imaging.**

I. Introduction

RADAR imaging exploits electromagnetic signals to characterize the investigated scene [1]. This technology has practical implications in a broad range of applications, including remote sensing [2], subsurface imaging [3], [4], biomedical imaging [5], through-wall imaging [6], [7], [8], passive radar imaging [10], [11], and target localization and tracking [8], [9].

In most cases, the raw radar data are not easily interpretable and a focusing step is mandatory to obtain a reliable image of the investigated domain. Focusing algorithms are mostly based on linearized models of the electromagnetic scattering phenomenon [12]. Popular examples include delay and sum beamforming [13], [14], migration [15], [16], diffraction tomography [17], [18], linearized microwave tomography approaches (e.g., see [4], [19], [20], [21]), and sparsity and compressed sensing algorithms [22], [23], [24], [25], [26], [27]. The aforementioned algorithms are known to provide only qualitative information about the probed targets in terms of position and approximate shape. However, unlike nonlinear inversion methods (e.g., see [28]), they are very efficient from the computation viewpoint, robust to noise on data, and uncertainness about the reference scenario, and they do not suffer from reliability problems caused by local minima [29].

A common feature of linear radar imaging strategies is the fact that they model only direct scattering returns from the targets, whereas multipath contributions due to target–environment and target–target interactions are neglected. As a result, when focusing the radar data with a linear algorithm, the resulting radar images can be affected by false targets, i.e., multipath ghosts, which completely impair the reconstructions [30]. In this respect, some ghost mitigation/identification strategies have been proposed based on subarray processing [30], [31], [32], [33], hidden Markov model [34], imaging dictionary [35], rotating array [36], and Hough transform [37]. It should be stressed that, under a priori knowledge of the scenario, multipath interactions between the target and the surrounding environment can also be exploited to enhance the imaging performance [38], [39], [40], [41], [42], [43].

In recent years, deep learning (DL) techniques, originally developed for image processing and computer vision tasks, are gaining increasing attention in the radar community due to their capability to solve effectively different tasks (e.g., detection, localization, classification, and denoising). As well known, these data-driven methods behave as universal approximators, i.e., they use training data to learn mapping a given input into a desired output. A representative but nonexhaustive list of research/survey papers in this field is given in [44], [45], [46], [47], [48], and [49].

In this article, we investigate the performance of the convolutional neural network (CNN) U-NET, originally developed for biomedical image segmentation [50] and later applied to inverse imaging problems [51], [52], to achieve multipath ghosts suppression in scenarios where the targets are small in terms of probing wavelength. Despite the possible generalization of the proposed clutter filtering strategy in different contexts (e.g., through-wall imaging), here we focus on the detection of metallic rebars via ground penetrating radar (GPR). This problem represents an interesting test bed since the targets are usually located very close to each other, and thus, the mutual interactions between them

Manuscript received 16 May 2023; revised 10 October 2023; accepted 11 November 2023. Date of publication 30 November 2023; date of current version 13 December 2023. *(Corresponding author: Gianluca Gennarelli.)*

The authors are with the Institute for Electromagnetic Sensing of the Environment (IREA), National Research Council of Italy (CNR), 80124 Naples, Italy (e-mail: gennarelli.g@irea.cnr.it).

Digital Object Identifier 10.1109/TGRS.2023.3337893

© 2023 The Authors. This work is licensed under a Creative Commons Attribution-NonCommercial-NoDerivatives 4.0 License.
For more information, see https://creativecommons.org/licenses/by-nc-nd/4.0/

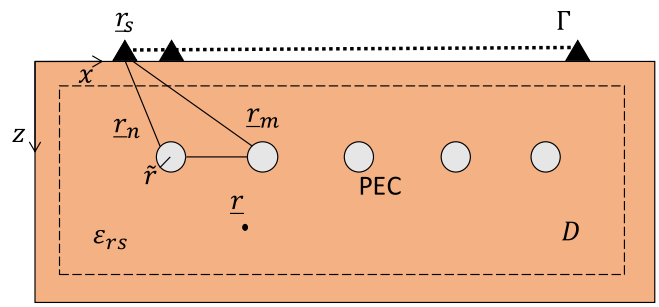

Fig. 1. Geometry of the radar imaging problem.

significantly affect the image quality. In the frame of GPR data processing, various machine/DL strategies have been recently proposed to characterize buried targets [53], [54], [55], retrieve permittivity maps [56], or perform decluttering of raw radargrams [57], [58], [59], [60]. As for decluttering, the available DL strategies do not focus on target–target interactions. Conversely, as a further novel contribution, the DL strategy here proposed works on tomographic images instead of radargrams. The network is trained on full-wave simulated data by taking into account different possible scenarios occurring in real applications. The effectiveness and robustness of the strategy are assessed on simulated data first and after through experimental tests.

This article is organized as follows. Section II describes the mathematical formulation of the radar imaging problem. Section III recalls the U-NET architecture and provides details on its implementation as well as on the dataset generation. Numerical and experimental results are reported in Sections IV and V, respectively. Conclusions follow in Section VI.

II. Radar Imaging Formulation

Let us consider the 2-D scenario shown in Fig. 1 where N perfectly conducting circular scatterers are located in a lossless and homogenous dielectric medium with relative dielectric permittivity ε_{rs}. The scene is probed by a monostatic GPR, i.e., by a transmitting (Tx) and receiving (Rx) antenna pair located at $\underline{r}_s$ and moving along the measurement line Γ at $z = 0$. The antennas are modeled as infinite electric line sources directed along y (TM polarization) and operating in the angular frequency band $\Omega = [\omega_{\min}, \omega_{\max}]$. We denote with $\underline{r}_n$ and $\underline{r}_m$ the positions of target n and m, respectively. Moreover, $\underline{r}$ is the position of a generic point within the investigation domain D.

The targets are thin cylinders, i.e., their radius $\tilde{r}$ is small in terms of the probing wavelength. In this case, they can be approximately treated as point targets and their scattered field can be written as

$$E_s\left(\underline{r}_s, \omega\right) \approx E_s^{\text{lin}}\left(\underline{r}_s, \omega\right) + E_s^{\text{mult}}\left(\underline{r}_s, \omega\right) \tag{1}$$

where E_s^{lin} accounts for the direct scattering contributions and E_s^{mult} refers to the multipath due to the mutual interactions between the targets. By considering only the first- and second-order contributions, (1) is rewritten as [30]

$$E_s\left(\underline{r}_s, \omega\right) \approx \sum_{n=1}^{N} a_n e^{-j2kR_n} + \sum_{\substack{n,m=1\\ n\neq m}}^{N} b_{nm} e^{-jk(R_n+R_m+R_{nm})} \tag{2}$$

where $k = (\omega/c)$ is the propagation constant in the medium (c is the wave speed); a_n is a complex coefficient accounting for the impinging field; $R_{n,m} = |\underline{r}_{n,m} - \underline{r}_s|$ are the distances between the measurement point $\underline{r}_s$ and the targets n and m, respectively; $R_{nm} = |\underline{r}_m - \underline{r}_n|$ is the distance between targets m and n, and b_{nm} is the amplitude of the multipath term.

The linear model accounts only for the direct scattering contributions and expresses the scattered field E_s as

$$E_s\left(\underline{r}_s, \omega\right) \approx \sum_{n=1}^{N} a_n e^{-j2kR_n}. \tag{3}$$

By adopting the linear distribution approach in [61], [62], and [63], (3) is rewritten as

$$E_s\left(\underline{r}_s, \omega\right) = \int_D e^{-j2k|\underline{r}-\underline{r}_s|}\gamma(\underline{r})d\underline{r} = L\gamma \tag{4}$$

where the unknown

$$\gamma(\underline{r}) = \sum_{n=1}^{N} \delta(\underline{r} - \underline{r}_n) \tag{5}$$

is the superposition of Dirac δ distributions having the support coincident with the targets' position.

Therefore, the radar imaging problem is formulated as the inversion of the linear integral equation in (4), where the operator L acts on a distribution space. An extension of the singular value decomposition (SVD) approach to the regularized inversion of linear operators acting on distribution spaces has been reported in [61], [62], and [63].

A truncated SVD (TSVD) inversion strategy is exploited and the retrieved solution is expressed as [64]

$$\tilde{\gamma} = \sum_{p=1}^{P_t} \frac{\langle E_s, u_p\rangle}{\sigma_p} v_p. \tag{6}$$

In the formula above, $\{u_p, \sigma_p, v_p\}_{p=1}^{\infty}$ is the singular spectrum of the operator L in (4), where σ_p are the singular values, u_p are the singular functions in the data space, and v_p are the singular functions in the unknown space. The truncation index P_t acts as a regularization parameter and is fixed in such a way as to achieve a suitable tradeoff between resolution and stability of the solution. The amplitude of the retrieved solution $\tilde{\gamma}$, as normalized to its maximum value, defines a spatial map, here referred to as a tomographic image and denoted by I, wherein the targets appear as focused spots.

It is worth pointing out that, by inverting the data in (1) via TSVD, the retrieved solution is written as

$$\begin{aligned}\tilde{\gamma} &= \tilde{\gamma}^{\text{lin}} + \tilde{\gamma}^{\text{mult}}\\ &= \sum_{p=1}^{P_t} \frac{\left\langle E_s^{\text{lin}}, u_p\right\rangle}{\sigma_p} v_p + \sum_{p=1}^{P_t} \frac{\left\langle E_s^{\text{mult}}, u_p\right\rangle}{\sigma_p} v_p.\end{aligned} \tag{7}$$

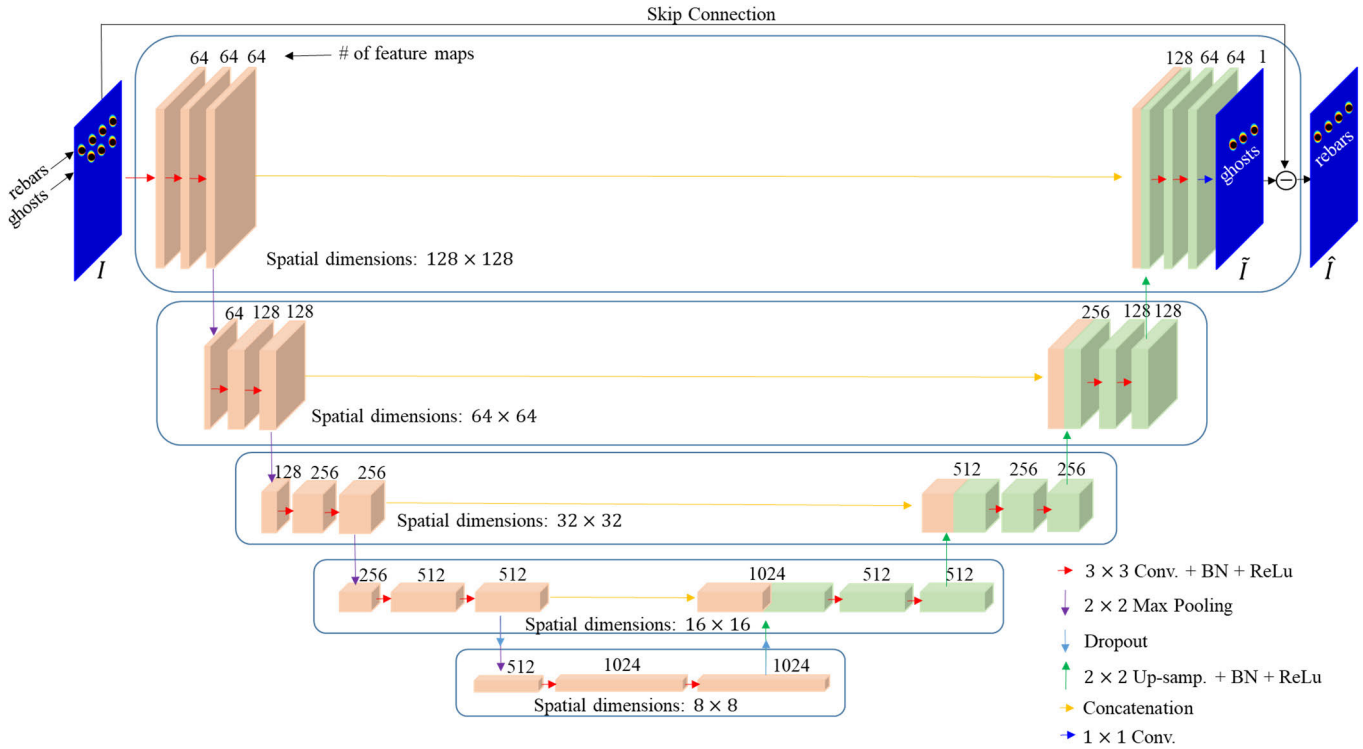

Fig. 2. Block diagram of the U-NET architecture for ghost removal in tomographic images.

Therefore, the tomographic image defined by (7) accounts not only for the linear term $\tilde{\gamma}^{\text{lin}}$ but also for the multipath one $\tilde{\gamma}^{\text{mult}}$, which is responsible for the presence of multipath ghosts affecting the reliability of the image.

The suppression of the multipath ghosts is the main scope of the DL strategy detailed in Section III.

III. Deep Learning-Based Ghost Filtering

A. U-NET Architecture

U-NET is a CNN characterized by a symmetric encoder–decoder architecture [50]. According to Fig. 2, the encoder (left side) extracts features from the input cluttered image I through a series of convolutional and pooling layers that gradually reduce data dimension while increasing the number of feature maps. The decoder (right side) provides a ghost-free image $\hat{I}$ from the encoded features through the use of a series of upsampling and convolutional layers that gradually increase the spatial resolution of the encoded features while reducing the number of feature maps. The network architecture is organized into five levels and is analogous to the one presented in [51]. In the encoding path, the input image I with size 128×128 undergoes a series of three 3×3 convolutions, each one followed by a batch normalization (BN) and rectified linear unit (ReLu) activation function (red arrows in Fig. 2). Each convolutional layer extracts several feature maps that increase in the lower network levels. Note that the image size is not decreased after each convolution operation because zero padding is adopted. A 2×2 max pooling (violet arrows) halves the spatial dimension of each feature map when passing from one level to the subsequent one. From the second level up to the bottom one, the number of convolutions decreases to two per level, each one still followed by a BN, ReLu activation function, and max pooling. A dropout layer (light blue arrow) randomly setting to zero a given percentage of the layer inputs [65] is exploited between the fourth and fifth levels (in both encoding and decoding paths) to prevent the network from overfitting. At the bottom level, the size of the feature maps is equal to 8×8.

The ascending path of U-NET starts with a 2×2 upsampling operation that doubles the size of each feature map followed by BN and ReLu (green arrow). Half of the feature maps are stacked (yellow arrow) with the corresponding cropped feature maps coming from the descending path, and then, a set of two 3×3 convolutions, BN, and ReLU is applied. Following this logic, it is possible to come back to the first network level. Here, a 1×1 convolution is applied to transform the feature maps into a single image $\tilde{I}$, which is subtracted from the input image I via the skip connection. In this way, residual learning is performed to mitigate the vanishing gradient problem [66]. In other words, the network learns to image the ghosts through the feature map $\tilde{I}$, which is subsequently subtracted from the input image to perform ghosts' filtering.

B. Learning Strategy and Implementation Details

The network is trained by providing a dataset consisting of image pairs (I, I^{gt}), where I is the image with ghosts and I^{gt} is a ground truth ghost-free image. As stated in Section II, the radii of the rebars are small in terms of the wavelength; therefore, their reconstruction can be approximated in terms

TABLE I
U-NET TRAINING OPTIONS AND HYPERPARAMETER SETTINGS

Option/Parameter	Description/Value
Optimizer	ADAM
Initial learning rate	1e-4
Learning rate schedule	piecewise
Learning rate drop period	10
Learning rate drop factor	0.5
Mini-batch size	4
Gradient threshold method	absolute-value
Gradient threshold	0.01
L_2 regularization parameter	1e-4
Dropout probability	0.4
Shuffle	every-epoch
Max. number of epochs	80

of the system point spread function (PSF). More specifically, if N rebars are located at positions $\underline{r}_n$, $n = 1, \ldots, N$, the ghost-free image I^{gt} can be formulated as the superposition of the TSVD-based PSFs located at the targets' positions, i.e.,

$$I^{\text{gt}}(\underline{r}) = \left| \sum_{n=1}^{N} \sum_{p=1}^{P_t} v_p(\underline{r}) v_p^*(\underline{r}_n) \right| \tag{8}$$

where $*$ denotes the conjugation operation. Note that assuming as ground truth, the image defined in (8), as normalized to its maximum value, allows us to facilitate the U-NET training. The PSFs, indeed, look more similar to the input tomographic reconstructions than the images showing a collection of point scatterers located at the targets' positions.

The loss function minimized during the training is half the squared error averaged over the mini-batch

$$\text{loss} = \frac{1}{P} \sum_{p=1}^{P} \frac{1}{2} \sum_{q=1}^{Q} \left| \hat{I}_{pq} - I_{pq}^{\text{gt}} \right|^2 \tag{9}$$

where $Q = 128 \times 128$ denotes the number of pixels in the images I_p and I_p^{gt}, and p linearly indexes the mini-batch with size P.

The training options and hyperparameters' settings are summarized in Table I. Specifically, the ADAptive Moment estimation (ADAM) optimizer is chosen to operate with data mini-batches of size 4. An adaptive learning rate halving every ten epochs is set and the clipping value for the gradient is equal to 0.02. L_2 regularization with parameter 1e^{-4} is set to limit network overfitting and data shuffling is carried out every epoch up to a maximum number of 80 epochs.

C. Dataset Generation

A synthetic dataset used for training, validation, and testing of U-NET is built by running 2-D simulations with the full-wave electromagnetic solver GPRMax based on the finite-difference time-domain (FDTD) method [67]. The goal of the simulations is to reproduce possible scenarios arising when performing GPR prospections on media containing metallic rebars. Fig. 3 shows the reference geometry used for the generation of the dataset. It is assumed that metallic rebars have the same radius $\tilde{r}$ and are all located at the same depth d from the air–medium interface. Moreover, x_0 is the horizontal

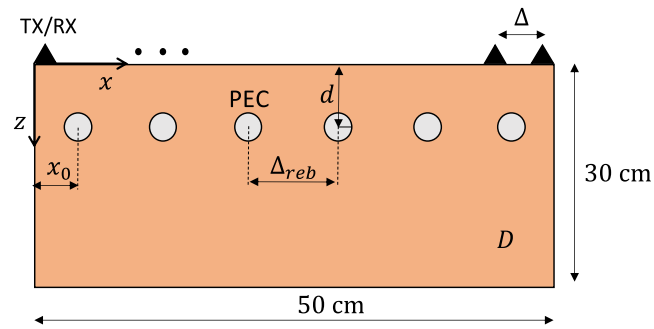

Fig. 3. Reference geometry considered for generating the synthetic dataset.

offset between the first measurement point and the first rebar, while Δ_{reb} is the spacing between the rebars' centers. The measurement line at the air–medium interface ($z = 0$ cm) is 50 cm long and sampled with a uniform step $\Delta = 2$ cm. At each point, a Ricker wavelet with a center frequency of 2 GHz is radiated into the medium and the received radar echo is recorded over the time window [0, 20] ns. The investigation domain $D = [0, 50] \times [0, 30]$ cm^2 is discretized into square cells with a size of 0.5 cm.

To ensure a sufficiently large diversity of the investigated scenarios, the electromagnetic and geometrical parameters involved in the simulations are varied as follows:

1) five random values for ε_{rs} uniformly chosen in the range [3, 10];
2) three different values of the electric conductivity of the medium, i.e., $\sigma_s = 0.001, 0.005, 0.01$ S/m;
3) five random values of rebars' depth d uniformly chosen in the range [5.0, 15.0] cm;
4) six values for the rebars' spacing Δ_{reb} uniformly spaced in the range [6.0, 16.0] cm;
5) three random values for the offset x_0 uniformly chosen in the interval [5.0, 10.0] cm.

The rebars are modeled as cylindrical PEC targets with a radius $\tilde{r} = 0.4$ cm. The combination of parameters x_0 and Δ_{reb} results in a number of rebars N variable in the range [3, 6]. Moreover, the combination of all the aforementioned geometrical and electromagnetic parameters produces a dataset of 1350 samples. This dataset is partitioned as follows: 1080 samples are used for network training, 135 samples are used for validation, and the remaining 135 samples are for testing. It is stressed that the dataset generation considers a realistic range of parameters arising in real GPR surveys. For instance, the electromagnetic properties (permittivity and conductivity) of the hosting medium can model different types of materials such as soil and concrete (see [3]). The geometrical properties of the rebars are also chosen by accounting for parameter values found in real-life applications.

To generate the tomographic image I, the raw radargrams are first processed in the time domain to remove the direct coupling between the antennas and the reflection from the air–medium interface. More specifically, after a zero-time setting at 0.7 ns, a time gating is performed by setting to zero the early time response of the radargram up to 1.4 ns. After, the filtered data are transformed in the frequency domain over the interval [1000, 3000] MHz with a step of 50 MHz and inverted

via TSVD. The TSVD regularization parameter P_t in (6) is set in such a way as to filter out the singular values lower than 20 dB with respect to the maximum one. As regards the ground truth image I^{gt}, (8) is evaluated by considering the rebar centers as the positions of the corresponding point targets. It must be pointed out that, based on the adopted discretization step of the investigation domain D, the dimension of the images I and I^{gt} is equal to 101×61. Therefore, a resampling based on a bicubic interpolation is carried out to convert the images into the 128×128 format required by U-NET (see Fig. 2). Both images I and I^{gt} are normalized with respect to their maximum.

D. Testing

Different metrics are adopted to evaluate quantitatively the performance of the trained network. In particular, the error between a predicted image $\hat{I}$ in the test dataset and the corresponding ground truth I^{gt} is expressed in terms of the root-mean-square error (RMSE)

$$\mathrm{RMSE} = \sqrt{\frac{1}{Q}\sum_{q=1}^{Q}\left|\hat{I}_q - I_q^{\mathrm{gt}}\right|^2} \tag{10}$$

and mean percentage error (MPE)

$$\mathrm{MPE} = 100\frac{\sum_{q=1}^{Q}\left|\hat{I}_q - I_q^{\mathrm{gt}}\right|^2}{\sum_{q=1}^{Q}\left|I_q^{\mathrm{gt}}\right|^2}. \tag{11}$$

A further figure of merit quantifying the overall enhancement in terms of signal-to-clutter ratio (SCR) is the improvement factor (IF)

$$\mathrm{IF} = 10\log_{10}\left(\frac{P_{\mathrm{target,output}}/P_{\mathrm{clutter,output}}}{P_{\mathrm{target,input}}/P_{\mathrm{clutter,input}}}\right) \tag{12}$$

where P_{target} is the power in the regions of the rebars (target power) and P_{clutter} is that outside (clutter). The notations input and output refer to the image at the input and the output of the network, respectively. The complete definition of the IF parameter is available in [30] and is skipped here for brevity. The regions of interest for the computation of target and clutter powers are squares centered on the rebars and having sides equal to $4\tilde{r}$.

E. Computation Details

The tomographic inversion algorithm is implemented under MATLAB 2020b on a Desktop PC equipped with an Intel Xeon Gold 6136 CPU (3.0-GHz clock frequency) and 256-GB RAM. The computation time required by tomographic imaging is due to the scattering operator L in (4) and its SVD, which take about 1 and 2.4 s, respectively. These quantities need to be calculated only once for every sample in the dataset. The formation of a tomographic reconstruction via TSVD is also very fast and takes about 0.02 s.

The network is trained and evaluated by using the MATLAB Deep Learning Toolbox on an NVIDIA Quadro GPU graphic processor equipped with 2304 CUDA[1] cores and 8-GB GDDR6 memory. The computation time involved in the training stage strongly varies with the size of the dataset (see Section IV). On the other hand, the time required for testing varies linearly with the size of the test dataset. In particular, the time needed by the network to produce the output from a single tomographic image at the input is very small and approximately equal to 0.2 s.

[1]Registered Trademark.

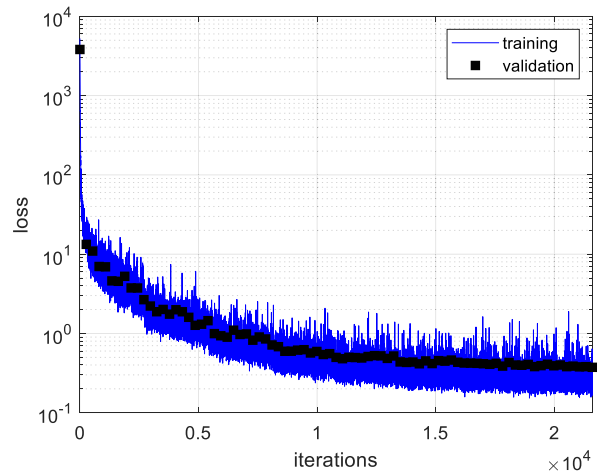

Fig. 4. Trend of training and validation loss versus number of iterations.

IV. Numerical Tests

A. Network Trained With Noiseless Data

The network is trained using the 1080 images dataset achieved from noiseless data. Fig. 4 shows the training progress in terms of training and validation loss versus the number of iterations. As can be observed, the curves are consistent and the loss values almost converge after 21 600 iterations for a total computation time of about 1.2 h.

The images shown in Fig. 5 allow visualization of the network operation through five samples randomly chosen from the test dataset. The first, second, third, and fourth rows represent the inputs, the learned feature maps, the outputs, and the ground truth images, respectively. As expected, the input tomographic images are corrupted in a more or less severe way by the presence of multipath ghosts. In some cases (e.g., test 1), the ghost targets are intense and very close to the true targets (black circles), thus becoming indistinguishable. It is worth noting that the learned feature maps shown in the panels on the second row are characterized by the presence of minima in correspondence with the true rebars' positions and this means that the network learns how to reconstruct the ghosts. As a result, the learned feature maps can be effectively subtracted from the cluttered input tomographic images producing ghost-free reconstructions. The effectiveness of the ghosts' filtering is also confirmed by the good agreement with the corresponding ground truth images.

The graphs plotted in Fig. 6 show the trends of the RMSE (left panel), MPE (middle panel), and IF (right panel) for each sample in the test dataset together with their mean value and standard deviation. In particular, the low mean error values (e.g., MPE = 0.5%) confirm that the network predictions

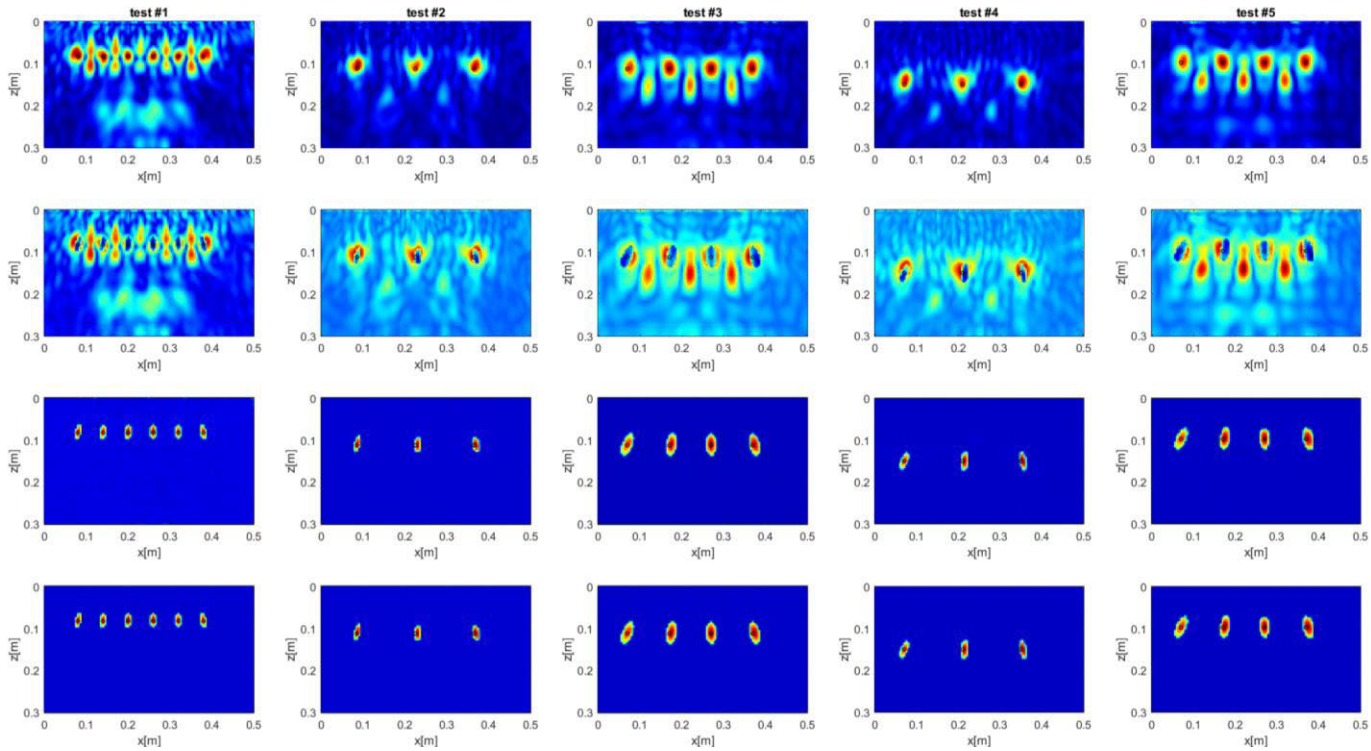

Fig. 5. Representative examples randomly selected from the noiseless test dataset. Input images (first row). Learned feature maps (second row). Output images (third row). Ground truth images (fourth row). The rebars are denoted by black circles. The color scale is [0, 1].

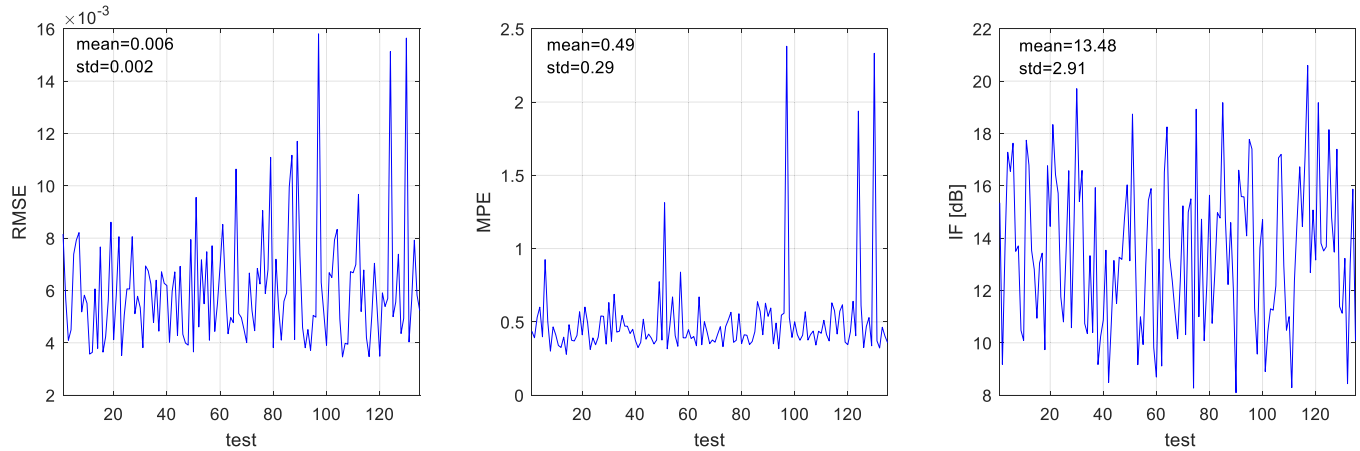

Fig. 6. Curves of RMSE (left panel), MPE (middle panel), and IF (right panel) for each sample in the test dataset. The mean and standard deviations of each parameter over the test dataset are included in each figure.

reproduce quite well the ground truths; at the same time, the average IF around 13.5 dB confirms the image quality enhancement in terms of SCR.

Starting from the network trained on noiseless data, a robustness analysis versus noise level is carried out. In detail, the original frequency domain scattered field data are corrupted by additive white Gaussian noise (AWGN) for signal-to-noise ratio (SNR) values equal to 20, 10, and 0 dB. Therefore, after TSVD inversion [see (6)], test datasets each composed of 135 image pairs are built for each SNR level.

The images plotted in Fig. 7 refer to five samples when SNR = 0 dB. As can be noticed, the input images are now more cluttered due to the combined effect of the multipath ghosts and the noise. On the other hand, apart from some residual clutter (see test 1), the images at the output of the network are improved considerably and quite similar to the ground truth.

A quantitative analysis of the network performance is carried out with the aid of Table II, which summarizes the mean values and the standard deviations of the considered metrics for each SNR level. According to the achieved data, it turns out that both mean RMSE and MPE increase with the noise level together with their corresponding standard deviations. Notably, the mean MPE increases from 0.49% to 7.71%, which means that the output images reproduce the ground truth ones less reliably. On the other hand, the mean IF

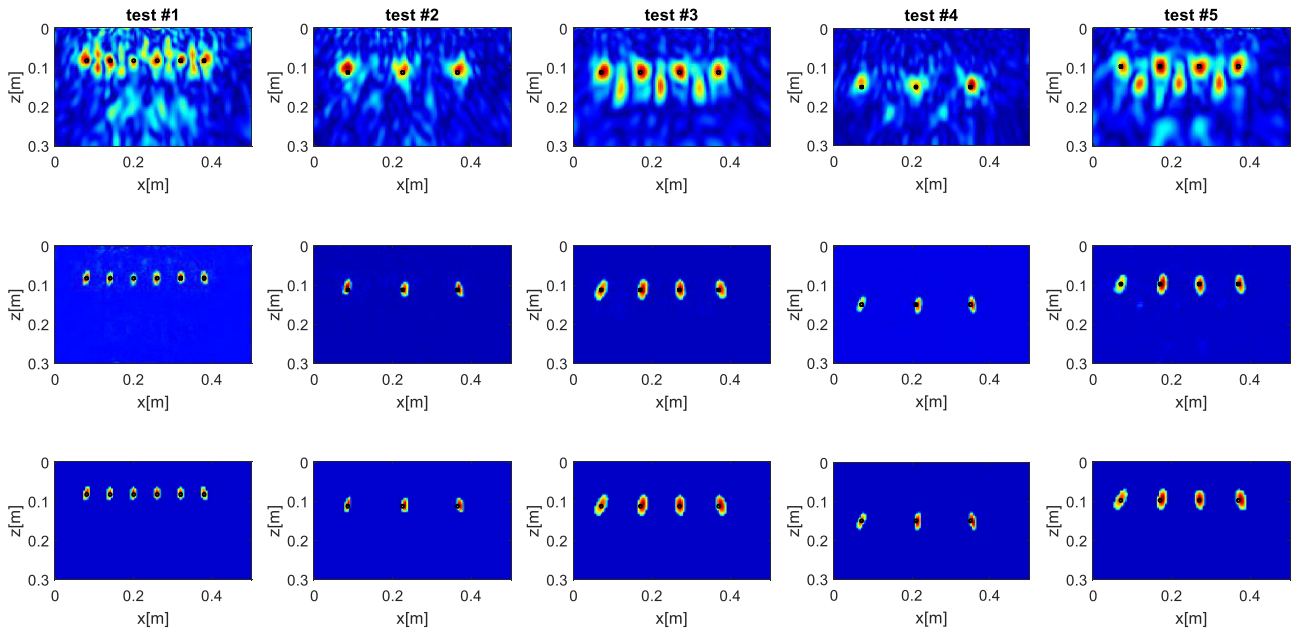

Fig. 7. Representative examples randomly selected from the noisy test dataset with SNR = 0 dB. Input images (first row). Output images (second row). Ground truth images (third row). The rebars are denoted by black circles. The color scale is [0, 1].

TABLE II

STATISTICS OF PERFORMANCE METRICS FOR THE NETWORK TRAINED WITH THE NOISELESS DATASET

Test case/parameter	RMSE mean (std)	MPE [%] mean (std)	IF [dB] mean (std)
noiseless	6.1e-3 (2.3e-3)	0.49 (0.29)	13.48 (2.91)
SNR= 20 dB	6.4e-3 (2.3e-3)	0.55 (0.30)	13.51 (2.90)
SNR= 10 dB	8.7e-3 (2.6e-3)	1.04 (0.42)	13.75 (2.90)
SNR= 0 dB	2.5e-2 (7.5e-3)	7.71 (3.93)	15.21 (2.76)

increases by about 2 dB when considering noisy data with an SNR = 0 dB. This suggests that the network performs a more effective clutter/noise filtering even though it was trained on noiseless data. This outcome can be explained by considering that IF is a relative metric and the noise power in the input image [i.e., $P_{\text{clutter,input}}$ in (12)] is larger when SNR = 0 dB.

B. Network Trained With Noisy Data

This section aims to provide an assessment of the network performance when the presence of noise in the tomographic images is considered during the learning stage. To this aim, the original dataset of 1350 samples is augmented by adding AWGN to the scattered field data in the frequency domain with different SNR levels. In detail, an extended dataset is obtained via TSVD and organized as follows:

1) 1350 noiseless images;
2) 1350 images with SNR = 20 dB;
3) 1350 images with SNR = 10 dB;
4) 1350 images with SNR = 0 dB.

Therefore, the overall dataset is composed of 5400 image pairs and is partitioned in the following way: 4320 samples are used for training, 540 samples are used for validation, and 540 samples are used for testing. The training options and hyperparameters' settings are those previously introduced

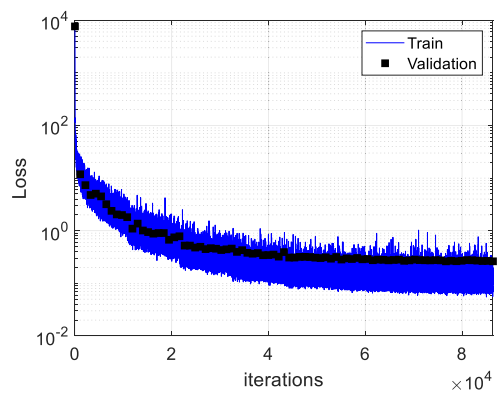

Fig. 8. Training and validation loss versus number of iterations for network trained with the extended data.

in Table I. The training and validation loss shown in Fig. 8 confirms that the solver has essentially converged in 86 400 iterations for a total computation time of around 7.12 h.

Similar to the validation carried out in Section IV-A, the network trained with the extended dataset is tested by considering 135 test image pairs each one characterized by a specific SNR level. For the sake of brevity, here we show only representative examples referred to the case SNR = 0 dB (see Fig. 9). By comparing the results in Fig. 9 with those achieved with the network trained on noiseless data (see Fig. 7), it emerges that the network is now able to filter also the minor residual clutter (e.g., see test #1). This claim is further corroborated by the values of the metrics summarized in Table III. As in the case of a network trained on noiseless data, the error and IF performance generally degrade as the SNR grows. However, unlike the network trained with noiseless data (see Table II), lower error values are attained when the SNR = 0 dB (e.g., MPE = 0.34%). As regards the

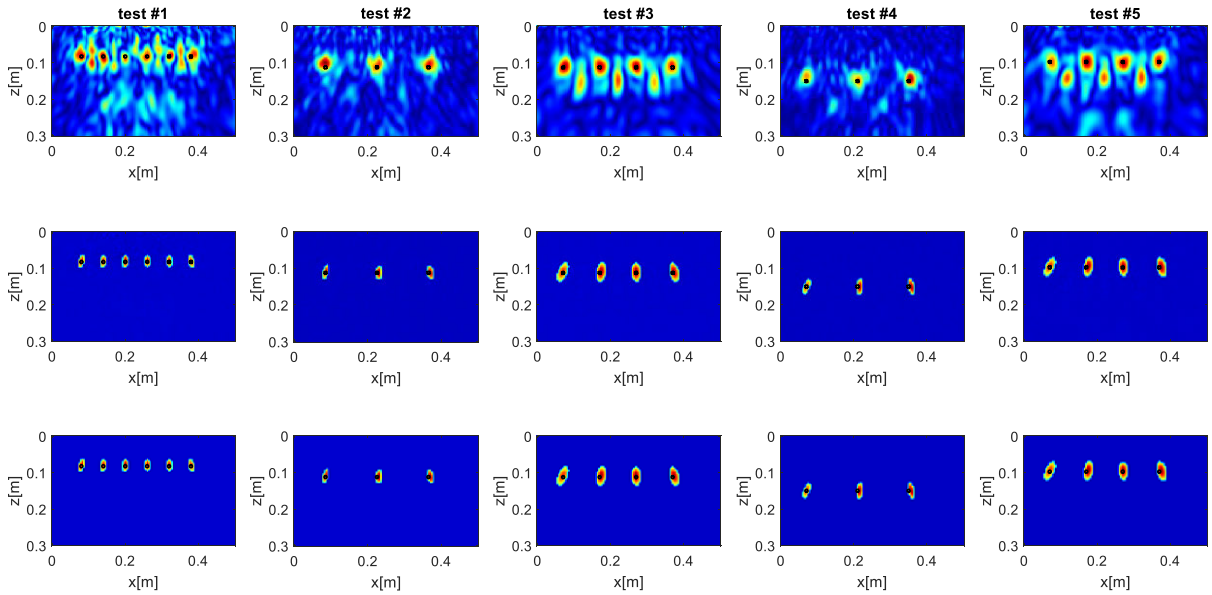

Fig. 9. Representative examples randomly selected from the noisy test dataset with SNR = 0 dB for the network trained with the extended dataset. Input images (first row). Output images (second row). Ground truth images (third row). The rebars are denoted by black circles. The color scale is [0, 1].

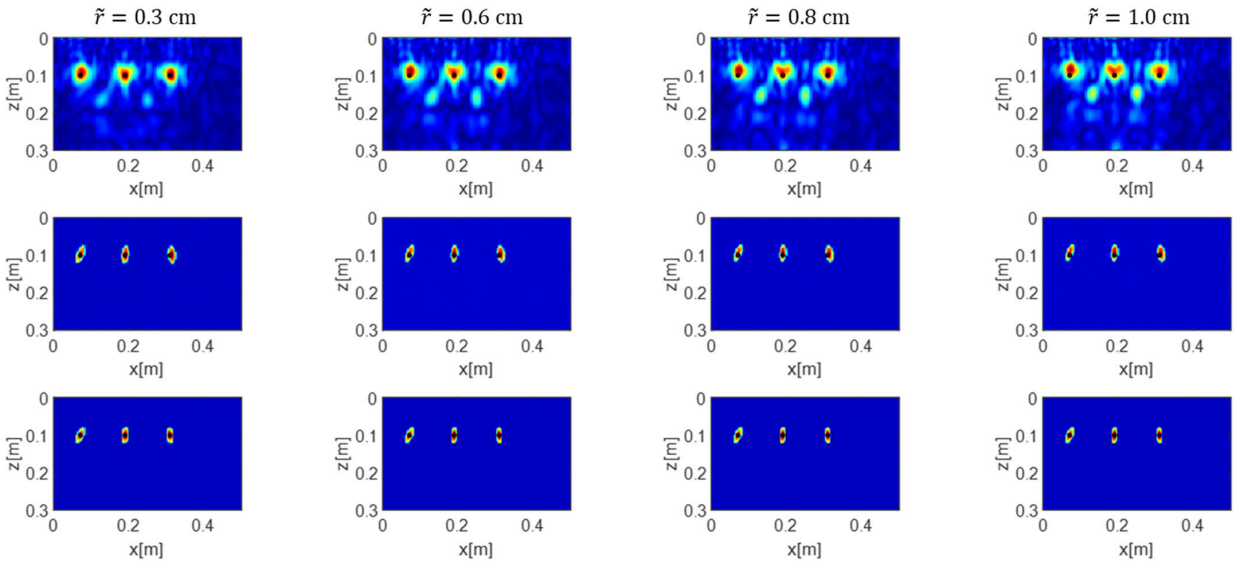

Fig. 10. Test examples corresponding to different rebar radii for the network trained with the extended dataset. Input images (first row). Output images (second row). Ground truth images (third row). The rebars are denoted by black circles. The color scale is [0, 1].

TABLE III

STATISTICS OF PERFORMANCE METRICS FOR THE NETWORK TRAINED WITH THE EXTENDED DATASET

Test case/parameter	RMSE mean (std)	MPE [%] mean (std)	IF [dB] mean (std)
noiseless	3.2e-3 (0.6e-3)	0.14 (0.04)	13.52 (3.01)
SNR= 20 dB	3.2e-3 (0.6e-3)	0.14 (0.04)	13.54 (3.02)
SNR= 10 dB	3.4e-3(0.7e-3)	0.16 (0.04)	13.67 (3.05)
SNR= 0 dB	4.7e-3(2.1e-3)	0.34 (0.33)	14.86 (3.26)

IF parameter, the attained values appear to be similar to their corresponding ones reported in Table II.

Given the above results, it is found that training the network with the extended dataset accounting also for noisy measurements allows for achieving a more robust noise filtering. For this reason, the latter network will be considered from this point on.

C. Tests in Novel Scenarios

In this section, we perform a robustness analysis aiming at investigating the generalization capabilities of the network in scenarios different from those it was trained on. Such an analysis allows conjecturing about the applicability of the proposed filtering strategy in real scenarios characterized by geometrical and/or electromagnetic parameters that may have not been considered during the training phase. More in detail, we consider novel test cases characterized by the following parameters:

1) $\varepsilon_{rs} = 5.5$.
2) $\sigma_s = 0.004$ S/m.

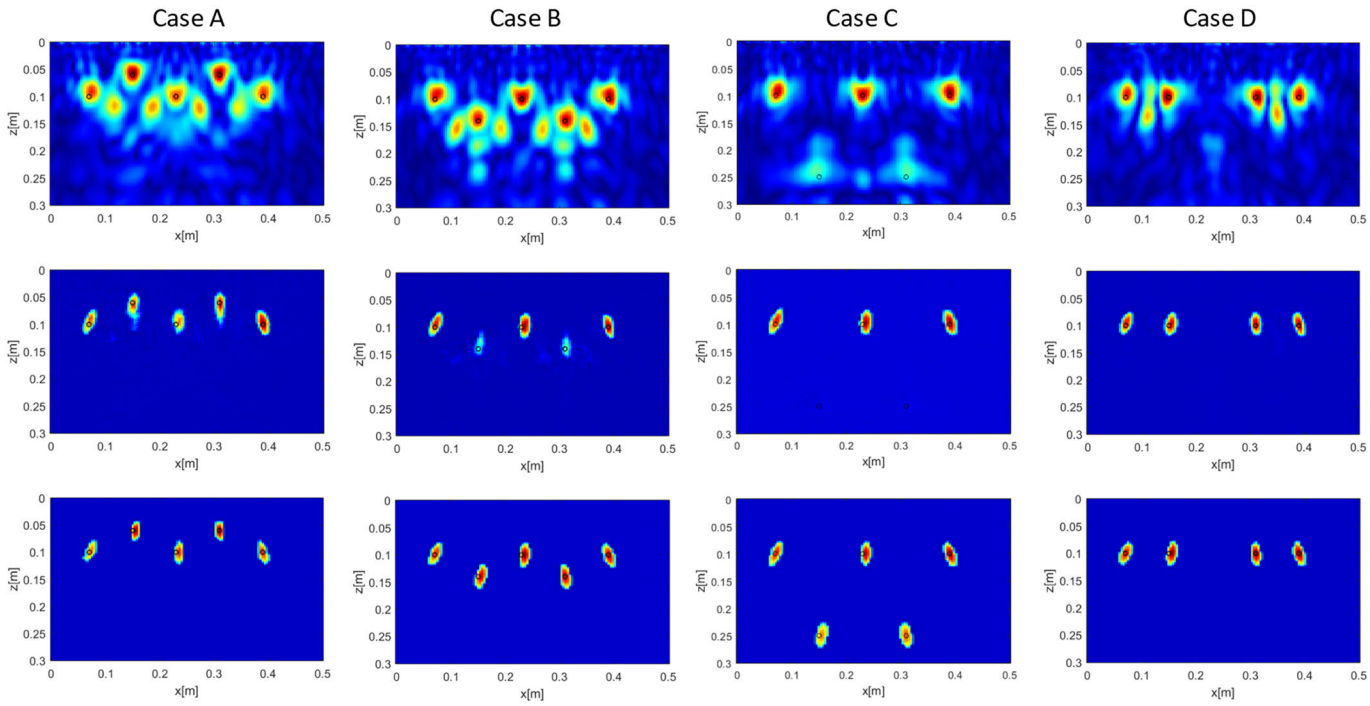

Fig. 11. Test examples with misaligned rebars (Cases A–C) and irregularly spaced rebars (Case D) for the network trained with the extended dataset. Input images (first row). Output images (second row). Ground truth images (third row). The rebars are denoted by black circles. The color scale is [0, 1].

3) $\Delta_{\text{reb}} = 12$ cm.
4) $x_0 = 7$ cm.
5) $d = 10$ cm;
6) $\tilde{r} = 0.3$, 0.6, 0.8, and 1.0 cm.
7) SNR = 10 dB.

Based on the above data, all the geometrical and electromagnetic parameters are different from those introduced in Section III-C. In particular, rebars' radii lower and greater than 0.4 cm are considered, while all remaining parameters are fixed in a deterministic way within the ranges considered in Section III-C.

The images depicted in Fig. 10 show the input, output, and ground truth images for the different values of the rebars' radius. Interestingly, it turns out that the network is still effective in suppressing the multipath ghosts for any $\tilde{r}$ value. This outcome is partly confirmed also by the values of the metrics summarized in Table IV. Indeed, despite the larger errors (MPE $\approx$ 44%) meaning that the network output does not reproduce well the ground truth from a quantitative perspective, the achieved IF values indicate that the clutter is filtered quite satisfactorily. The latter result is useful in applications where the main goals are target detection and localization.

In the following, we assess the robustness of the network trained with the extended dataset when the rebars are not all aligned along the depth. Specifically, we consider three representative cases where two out of five rebars are shifted upward by 4 cm (case A), downward by 4 cm (case B), and downward by 15 cm (case C) compared to the remaining rebars, which are located at a nominal depth of 10 cm. The same simulation parameters of the previous examples are considered save for the radius of the rebars which is set at 0.4 cm. As can be observed from Fig. 11, the network is quite robust and capable of discerning the rebars from the ghosts in the case of a small displacement (cases A and B) from the nominal depth even if it has been trained with aligned rebars. On the other hand, in the case of a large displacement (case C), the network suppresses the ghosts but also the deeper rebars. As a result, scenarios with large rebars' displacement should be addressed during the training stage to

TABLE IV
PERFORMANCE METRICS WITH THE EXTENDED DATASET VERSUS REBARS' RADII AND ARRANGEMENT

Test case/parameter	RMSE	MPE [%]	IF [dB]
$\tilde{r}$=0.3 cm	0.039	26.64	10.62
$\tilde{r}$=0.6 cm	0.044	35.15	11.22
$\tilde{r}$=0.8 cm	0.047	39.35	11.43
$\tilde{r}$=1.0 cm	0.050	44.23	11.47
Case A	0.042	26.22	11.53
Case B	0.052	27.63	12.05
Case C	0.065	44.70	10.86
Case D	0.033	13.29	12.51

Fig. 12. Photograph of the experimental setup showing the GPR antenna (left panel) and the rebars' arrangement (right panel).

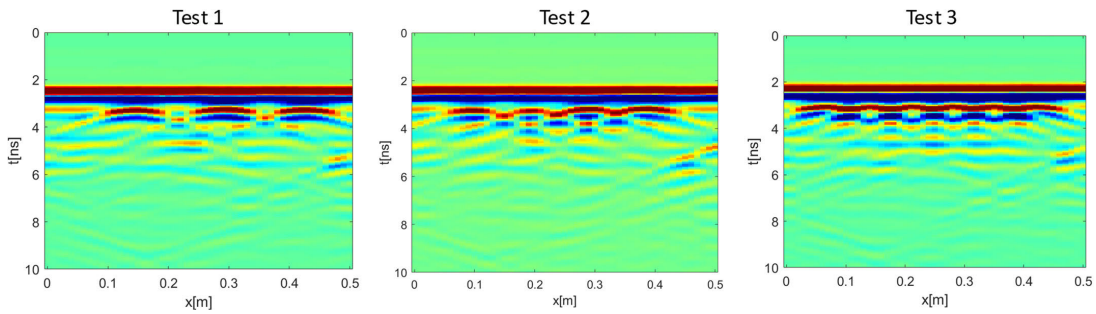

Fig. 13. Raw radargram recorded during Tests 1–3.

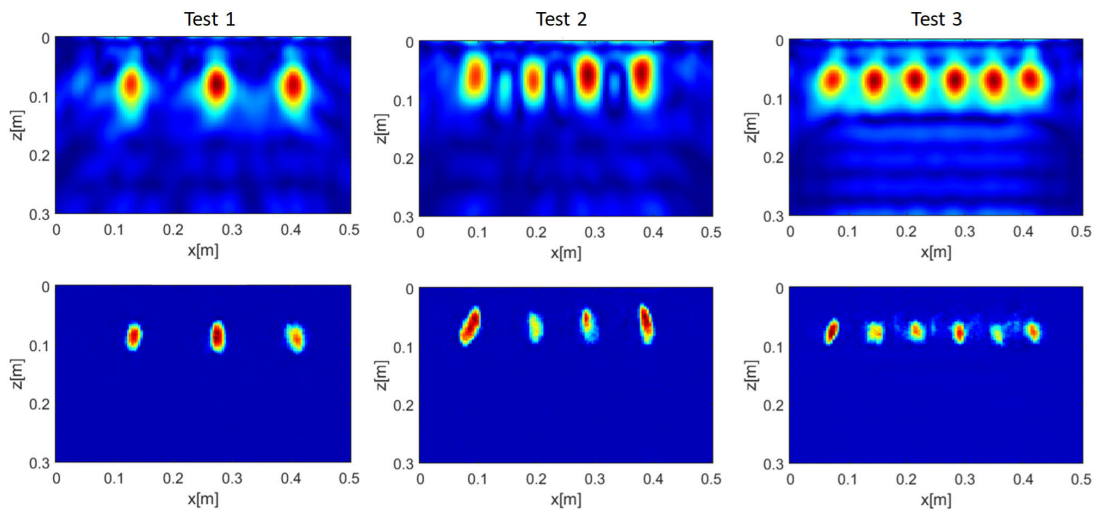

Fig. 14. Tomographic reconstructions related to Tests 1–3 for the network trained with the extended dataset. Input images (first row). Output images (second row). The color scale is [0, 1].

achieve proper ghosts' suppression. The IF values related to the above-described tests are listed in Table IV.

Finally, we examine the network operation when the rebars do not have a periodic arrangement (case D). To this aim, we consider a test featuring four rebars with a 4 cm radius buried at a depth of 0.1 m in a medium with the same electromagnetic features considered so far. As shown in Fig. 11, rebars 1 and 2 and 3 and 4 have a spacing of $\Delta_{\text{reb}} = 8$ cm, while rebars 2 and 3 have a spacing $\Delta_{\text{reb}} = 16$ cm. It can be observed in Fig. 11 that the multipath ghost between rebars 2 and 3 is located deeper than the other ones because of the larger spacing. However, by comparing the network output with the ground truth image, it can be concluded that the network still allows for achieving satisfactory ghosts' suppression.

V. Experimental Validation

This section aims to provide an experimental assessment of the proposed DL ghost removal strategy. Controlled tests have been performed at the Electromagnetic Diagnostics Laboratory of IREA-CNR. The tests involve the imaging of metallic rebars buried into a wood box of size 100 cm × 70 cm × 45 cm filled with dry soil up to a height of 17 cm from its bottom (see Fig. 12). As in the numerical experiments, we consider a variable number of rebars ($\tilde{r} = 0.4$ and 0.6 cm), which are all located at a depth of $d = 7.0$ cm below the air–soil interface.

The tests have been performed with the aid of the pulsed GPR system (IDS RIS Hi-Mode) equipped with the TR-HF antenna operating at the center frequency of 2 GHz. The antenna has been put in contact with the air–soil interface and manually moved along a 50-cm-long line to record scans every 1 cm in the fast time window [0, 16] ns.

The experimental conditions are detailed as follows:

1) *Test 1:* three rebars with $\tilde{r}$ =0.4 cm and $\Delta_{\text{reb}} = 14$ cm;
2) *Test 2:* four rebars with $\tilde{r} = 0.4$ cm and $\Delta_{\text{reb}} = 10$ cm;
3) *Test 3:* six rebars with $\tilde{r} = 0.4$ cm and $\Delta_{\text{reb}} = 7$ cm;
4) *Test 4:* three rebars with $\tilde{r} = 0.7$ cm and $\Delta_{\text{reb}} = 12$ cm;
5) *Test 5:* four rebars with $\tilde{r} = 0.7$ cm and $\Delta_{\text{reb}} = 10$ cm.

It must be noticed that Tests 1–3 refer to experimental conditions considered in the training phase; on the other hand, Tests 4 and 5 constitute a benchmark to appraise the generalization capability of the network for thicker rebars not considered during training.

The raw radargrams are processed in the time domain by setting the time zero at 2.1 ns and applying a time gating up to 2.8 ns. The filtered data are subsequently transformed in the frequency domain over the band [400, 2400] MHz with a step of 100 MHz. As regards the tomographic data processing, the soil permittivity is set at $\varepsilon_{\text{rs}} = 4$ in agreement with [68], the investigation domain $D = [0, 50] \times [0, 30]$ cm^2 is discretized with a spatial step of 0.5 cm, and the TSVD threshold is equal to −15 dB.

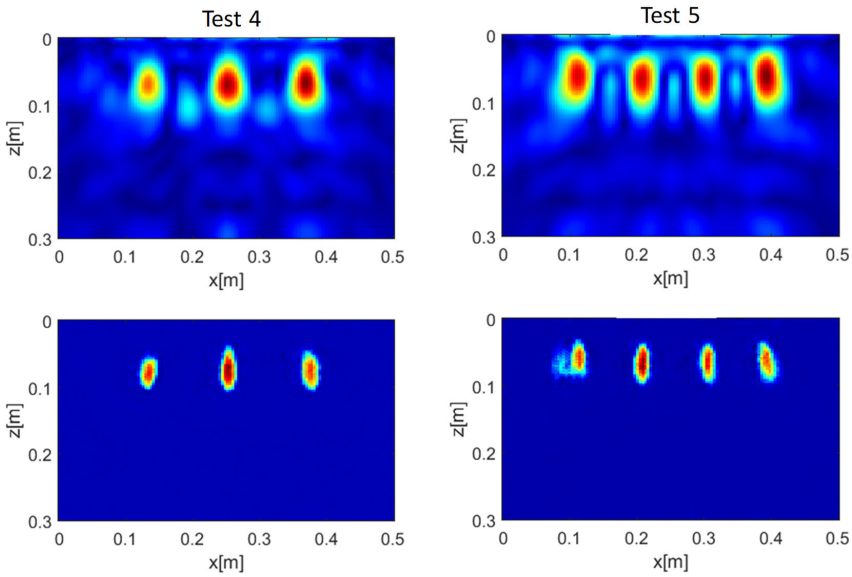

Fig. 15. Tomographic reconstructions related to Tests 4 and 5 for the network trained with the extended dataset. Input images (first row). Output images (second row). The color scale is [0, 1].

Fig. 16. Photograph of the archeological site and investigated structure in King's room.

Fig. 13 shows the radargrams referred to Tests 1–3. As expected, strong diffraction hyperbolas corresponding to the direct scattering echoes from the rebars are observed around $t = 3$ ns. Moreover, the weaker echoes arriving at later times originating from the interactions between the targets are responsible for the generation of multipath ghosts.

The reconstructions reported in the top panels of Fig. 14 are the tomographic images at the input of the network. As can be seen, more or less evident multipath ghosts appear in the neighborhood of the true targets (red spots). In this regard, the multipath ghosts in the image related to Test 3 are not visible because they cannot be resolved due to the limited horizontal resolution (around 3 cm) and the smaller target spacing ($\Delta_{\text{reb}} = 7$ cm). On the other hand, the tomographic images at the output of the network (bottom panels in Fig. 14) highlight that the multipath ghosts are effectively suppressed, thus allowing an unambiguous interpretation of the scene.

In Fig. 15, we report the results achieved while processing the GPR data referred to Tests 4 and 5 concerning the thicker rebars. Despite the network being trained with rebars having smaller radii, it turns out that it is equally effective in suppressing the multipath ghosts and increasing the image SCR. This claim is also corroborated by the values of the IF parameter summarized in Table V.

We conclude this section by providing an assessment of the proposed DL-based ghost removal strategy in the case of GPR data collected on the field. A measurement campaign was carried out at the Knossos Palace in Crete, Greece, in July 2018. Several pillars, columns, and concrete roof slabs of the East Wing ("Hall of Double Axes" and "Queen's Megaron") and of the "South House" were investigated, to identify the

TABLE V
IF VALUES FOR THE LABORATORY TESTS

Test	IF [dB]
1	27.8
2	24.4
3	23.5
4	27.1
5	26.1

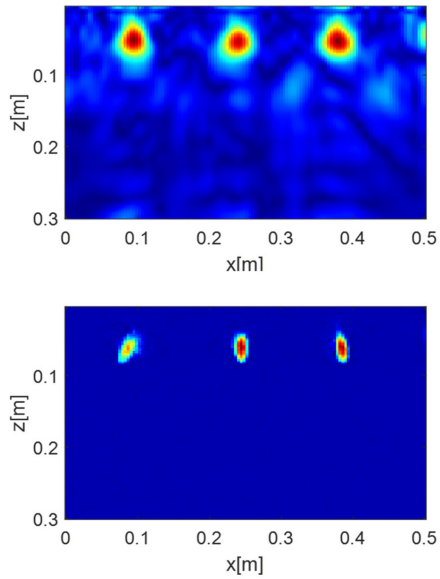

Fig. 17. Tomographic reconstruction of the investigated concrete roof slabs. Input image (top panel). Output image (bottom panel).

materials and restoration methods with a specific focus on rebars in reinforced concrete.

As a representative test case, Fig. 16 shows a 30-cm-thick concrete roof slab inspected with the previously described GPR system. The antenna was manually moved to gather data along a 50-cm-long line with a step of 1 cm. The raw data are processed by following the same steps used for the laboratory data with only a slight modification to some parameters, i.e., time zero at 4.25 ns and time gating up to 4.8 ns. The concrete permittivity is estimated as 6.5 based on the measured slab thickness and travel time analysis.

The image depicted in the top panel of Fig. 17 shows the tomographic reconstruction of the structure, which reveals the presence of three metallic rebars arranged with a spacing of 15 cm and approximately located at a depth of 6 cm. Furthermore, some multipath ghosts appear at a depth of around 13 cm. As no a priori information is available on the rebars' radius, it is not possible to establish if the experimental conditions are accounted for by training. Despite that, the output image highlights that the multipath ghosts are suppressed in a quite satisfactory way (IF = 10.5 dB).

VI. CONCLUSION

A supervised deep learning strategy has been developed for multipath ghost removal in linear microwave tomographic images. The proposed strategy is based on the CNN U-NET and assumes that the input is a tomographic image corrupted by ghosts, whereas the output is a ghost-free reconstruction based on the system PSF. An extensive set of numerical simulations based on synthetic full-wave data has been presented about the localization of metallic rebars via GPR. It has been demonstrated that the DL-based ghost filtering strategy is effective and robust to noise and changes in the parameters of the scenario. Furthermore, despite the training exclusively based on simulated data, experimental tests carried out in the laboratory and on the field have assessed the effectiveness of the proposed strategy. A further research activity will regard the combined use of U-NET and microwave tomography concepts in other radar imaging contexts. The proposed approach may be extended to multipath ghosts' suppression in through-wall scenarios offering the possibility to enhance ghosts' filtering in combination with other higher level signal processing algorithms (e.g., trackers). However, such an extension is not trivial and requires a modification of the training step to account for the additional challenges related to the size and the dynamic behavior of the targets. Future research will also focus on the determination of the optimal training strategy in the presence of a priori information on the noise level of the data.

REFERENCES

[1] M. Cheney and B. Borden, *Fundamentals of Radar Imaging*. Philadelphia, PA, USA: Society for Industrial and Applied Mathematics, 2009.

[2] J. Richards, *Remote Sensing With Imaging Radar*. Berlin, Germany: Springer, 2009.

[3] D. J. Daniels, *Ground Penetrating Radar*, vol. 1. Edison, NJ, USA: IET, 2004.

[4] I. Catapano, G. Gennarelli, G. Ludeno, C. Noviello, G. Esposito, and F. Soldovieri, "Contactless ground penetrating radar imaging: State of the art, challenges, and microwave tomography-based data processing," *IEEE Geosci. Remote Sens. Mag.*, vol. 10, no. 1, pp. 251–273, Mar. 2022.

[5] N. K. Nikolova, "Microwave imaging for breast cancer," *IEEE Microw. Mag.*, vol. 12, no. 7, pp. 78–94, Dec. 2011.

[6] M. G. Amin, *Through-the-Wall Radar Imaging*. Boca Raton, FL, USA: CRC Press, 2011.

[7] G. Gennarelli, G. Riccio, R. Solimene, and F. Soldovieri, "Radar imaging through a building corner," *IEEE Trans. Geosci. Remote Sens.*, vol. 52, no. 10, pp. 6750–6761, Oct. 2014.

[8] G. Gennarelli, G. Vivone, P. Braca, F. Soldovieri, and M. G. Amin, "Multiple extended target tracking for through-wall radars," *IEEE Trans. Geosci. Remote Sens.*, vol. 53, no. 12, pp. 6482–6494, Dec. 2015.

[9] M. G. Amin, *Radar for Indoor Monitoring*. Boca Raton, FL, USA: CRC Press, 2017.

[10] D. Pastina, F. Santi, F. Pieralice, M. Antoniou, and M. Cherniakov, "Passive radar imaging of ship targets with GNSS signals of opportunity," *IEEE Trans. Geosci. Remote Sens.*, vol. 59, no. 3, pp. 2627–2642, Mar. 2021.

[11] G. Gennarelli, M. G. Amin, F. Soldovieri, and R. Solimene, "Passive multiarray image fusion for RF tomography by opportunistic sources," *IEEE Geosci. Remote Sens. Lett.*, vol. 12, no. 3, pp. 641–645, Mar. 2015.

[12] R. Solimene, I. Catapano, G. Gennarelli, A. Cuccaro, A. Dell'Aversano, and F. Soldovieri, "SAR imaging algorithms and some unconventional applications: A unified mathematical overview," *IEEE Signal Process. Mag.*, vol. 31, no. 4, pp. 90–98, Jul. 2014.

[13] F. Ahmad, Y. Zhang, and M. G. Amin, "Three-dimensional wideband beamforming for imaging through a single wall," *IEEE Geosci. Remote Sens. Lett.*, vol. 5, no. 2, pp. 176–179, Apr. 2008.

[14] M. Dehmollaian, M. Thiel, and K. Sarabandi, "Through-the-Wall imaging using differential SAR," *IEEE Trans. Geosci. Remote Sens.*, vol. 47, no. 5, pp. 1289–1296, May 2009.

[15] J. M. Lopez-Sahcnez and J. Fortuny-Guasch, "3-D radar imaging using range migration techniques," *IEEE Trans. Antennas Propag.*, vol. 48, no. 5, pp. 728–737, May 2000.

[16] X. Zhuge, A. G. Yarovoy, T. Savelyev, and L. Ligthart, "Modified Kirchhoff migration for UWB MIMO array-based radar imaging," *IEEE Trans. Geosci. Remote Sens.*, vol. 48, no. 6, pp. 2692–2703, Jun. 2010.

[17] A. J. Devaney, "Geophysical diffraction tomography," *IEEE Trans. Geosci. Remote Sens.*, vol. GE-22, no. 1, pp. 3–13, Jan. 1984.

[18] W. Zhang and A. Hoorfar, "Three-dimensional real-time through-the-wall radar imaging with diffraction tomographic algorithm," *IEEE Trans. Geosci. Remote Sens.*, vol. 51, no. 7, pp. 4155–4163, Jul. 2013.

[19] R. Persico, R. Bernini, and F. Soldovieri, "The role of the measurement configuration in inverse scattering from buried objects under the born approximation," *IEEE Trans. Antennas Propag.*, vol. 53, no. 6, pp. 1875–1887, Jun. 2005.

[20] G. Gennarelli, G. Ludeno, I. Catapano, and F. Soldovieri, "Full 3-D imaging of vertical structures via ground-penetrating radar," *IEEE Trans. Geosci. Remote Sens.*, vol. 58, no. 12, pp. 8857–8873, Dec. 2020.

[21] G. Gennarelli, C. Noviello, G. Ludeno, G. Esposito, F. Soldovieri, and I. Catapano, "Three-dimensional ray-based tomographic approach for contactless GPR imaging," *IEEE Trans. Geosci. Remote Sens.*, vol. 61, 2023, Art . no. 2000614.

[22] R. Baraniuk and P. Steeghs, "Compressive radar imaging," in *Proc. IEEE Radar Conf.*, Waltham, MA, USA, Apr. 2007, pp. 128–133.

[23] Y.-S. Yoon and M. G. Amin, "Through-the-Wall radar imaging using compressive sensing along temporal frequency domain," in *Proc. IEEE Int. Conf. Acoust., Speech Signal Process.*, Dallas, TX, USA, Mar. 2010, pp. 2806–2809.

[24] L. C. Potter, E. Ertin, J. T. Parker, and M. Cetin, "Sparsity and compressed sensing in radar imaging," *Proc. IEEE*, vol. 98, no. 6, pp. 1006–1020, Jun. 2010.

[25] G. Gennarelli, I. Catapano, and F. Soldovieri, "RF/microwave imaging of sparse targets in urban areas," *IEEE Antennas Wireless Propag. Lett.*, vol. 12, pp. 643–646, 2013.

[26] M. Ambrosanio and V. Pascazio, "A compressive-sensing-based approach for the detection and characterization of buried objects," *IEEE J. Sel. Topics Appl. Earth Observ. Remote Sens.*, vol. 8, no. 7, pp. 3386–3395, Jul. 2015.

[27] M. T. Bevacqua and R. Scapaticci, "A compressive sensing approach for 3D breast cancer microwave imaging with magnetic nanoparticles as contrast agent," *IEEE Trans. Med. Imag.*, vol. 35, no. 2, pp. 665–673, Feb. 2016.

[28] M. Pastorino and A. Randazzo, *Microwave Imaging Methods and Applications*. Boston, MA, USA: Artech House, 2018.

[29] T. Isernia, V. Pascazio, and R. Pierri, "On the local minima in a tomographic imaging technique," *IEEE Trans. Geosci. Remote Sens.*, vol. 39, no. 7, pp. 1596–1607, Jul. 2001.

[30] G. Gennarelli and F. Soldovieri, "Multipath ghosts in radar imaging: Physical insight and mitigation strategies," *IEEE J. Sel. Topics Appl. Earth Observ. Remote Sens.*, vol. 8, no. 3, pp. 1078–1086, Mar. 2015.

[31] D. R. Obuchon, D. A. Garren, J. S. Goldstein, R. R. Greene, and J. A. North, "Drift inversion estimation of multipath ghosts in SAR image reconstruction," in *Proc. IEEE Radar Conf.*, Apr. 2004, pp. 556–558.

[32] W. Liang, H. Xiaotao, Z. Zhimin, and S. Qian, "Research on UWB SAR image formation with suppressing multipath ghosts," in *Proc. CIE Int. Conf. Radar*, Oct. 2006, pp. 1–3.

[33] G. Gennarelli, G. Vivone, P. Braca, F. Soldovieri, and M. G. Amin, "Comparative analysis of two approaches for multipath ghost suppression in radar imaging," *IEEE Geosci. Remote Sens. Lett.*, vol. 13, no. 9, pp. 1226–1230, Sep. 2016.

[34] Q. Tan, H. Leung, Y. Song, and T. Wang, "Multipath ghost suppression for through-the-wall radar," *IEEE Trans. Aerosp. Electron. Syst.*, vol. 50, no. 3, pp. 2284–2292, Jul. 2014.

[35] S. Guo, G. Cui, L. Kong, and X. Yang, "An imaging dictionary based multipath suppression algorithm for through-wall radar imaging," *IEEE Trans. Aerosp. Electron. Syst.*, vol. 54, no. 1, pp. 269–283, Feb. 2018.

[36] S. Guo, X. Yang, G. Cui, Y. Song, and L. Kong, "Multipath ghost suppression for through-the-wall imaging radar via array rotating," *IEEE Geosci. Remote Sens. Lett.*, vol. 15, no. 6, pp. 868–872, Jun. 2018.

[37] R. Feng, E. D. Greef, M. Rykunov, H. Sahli, S. Pollin, and A. Bourdoux, "Multipath ghost recognition for indoor MIMO radar," *IEEE Trans. Geosci. Remote Sens.*, vol. 60, 2022, Art. no. 5104610.

[38] R. J. Burkholder, "Electromagnetic models for exploiting multi-path propagation in through-wall radar imaging," in *Proc. Int. Conf. Electromagn. Adv. Appl.*, Turin, Italy, Sep. 2009, pp. 572–575.

[39] P. Setlur, M. Amin, and F. Ahmad, "Multipath model and exploitation in through-the-wall and urban radar sensing," *IEEE Trans. Geosci. Remote Sens.*, vol. 49, no. 10, pp. 4021–4034, Oct. 2011.

[40] M. Leigsnering, F. Ahmad, M. Amin, and A. Zoubir, "Multipath exploitation in through-the-wall radar imaging using sparse reconstruction," *IEEE Trans. Aerosp. Electron. Syst.*, vol. 50, no. 2, pp. 920–939, Apr. 2014.

[41] G. Gennarelli and F. Soldovieri, "Radar imaging through cinderblock walls: Achievable performance by a model-corrected linear inverse scattering approach," *IEEE Trans. Geosci. Remote Sens.*, vol. 52, no. 10, pp. 6738–6749, Oct. 2014.

[42] P. Setlur, T. Negishi, N. Devroye, and D. Erricolo, "Multipath exploitation in non-LOS urban synthetic aperture radar," *IEEE J. Sel. Topics Signal Process.*, vol. 8, no. 1, pp. 137–152, Feb. 2014.

[43] S. Guo, G. Cui, L. Kong, Y. Song, and X. Yang, "Multipath analysis and exploitation for MIMO through-the-wall imaging radar," *IEEE J. Sel. Topics Appl. Earth Observ. Remote Sens.*, vol. 11, no. 10, pp. 3721–3731, Oct. 2018.

[44] E. Mason, B. Yonel, and B. Yazici, "Deep learning for radar," in *Proc. IEEE Radar Conf. (RadarConf)*, Seattle, WA, USA, May 2017, pp. 1703–1708.

[45] Y. Li, C. Peng, Y. Chen, L. Jiao, L. Zhou, and R. Shang, "A deep learning method for change detection in synthetic aperture radar images," *IEEE Trans. Geosci. Remote Sens.*, vol. 57, no. 8, pp. 5751–5763, Aug. 2019.

[46] Z. Tong, J. Gao, and D. Yuan, "Advances of deep learning applications in ground-penetrating radar: A survey," *Construct. Building Mater.*, vol. 258, Oct. 2020, Art. no. 120371.

[47] G. Fracastoro, E. Magli, G. Poggi, G. Scarpa, D. Valsesia, and L. Verdoliva, "Deep learning methods for synthetic aperture radar image despeckling: An overview of trends and perspectives," *IEEE Geosci. Remote Sens. Mag.*, vol. 9, no. 2, pp. 29–51, Jun. 2021.

[48] Z. Geng, H. Yan, J. Zhang, and D. Zhu, "Deep-learning for radar: A survey," *IEEE Access*, vol. 9, pp. 141800–141818, 2021.

[49] A. H. Oveis, E. Giusti, S. Ghio, and M. Martorella, "A survey on the applications of convolutional neural networks for synthetic aperture radar: Recent advances," *IEEE Aerosp. Electron. Syst. Mag.*, vol. 37, no. 5, pp. 18–42, May 2022.

[50] O. Ronneberger, P. Fischer, and T. Brox, "U-Net: Convolutional networks for biomedical image segmentation," in *Proc. 18th Int. Conf. Med. Image Comput. Comput.-Assist. Intervent. (MICCAI)*, Munich, Germany, Oct. 2015, pp. 234–241.

[51] K. H. Jin, M. T. McCann, E. Froustey, and M. Unser, "Deep convolutional neural network for inverse problems in imaging," *IEEE Trans. Image Process.*, vol. 26, no. 9, pp. 4509–4522, Sep. 2017.

[52] Z. Wei and X. Chen, "Deep-learning schemes for full-wave nonlinear inverse scattering problems," *IEEE Trans. Geosci. Remote Sens.*, vol. 57, no. 4, pp. 1849–1860, Apr. 2019.

[53] I. Giannakis, A. Giannopoulos, and C. Warren, "A machine learning scheme for estimating the diameter of reinforcing bars using ground penetrating radar," *IEEE Geosci. Remote Sens. Lett.*, vol. 18, no. 3, pp. 461–465, Mar. 2021.

[54] X. Li, H. Liu, F. Zhou, Z. Chen, I. Giannakis, and E. Slob, "Deep learning-based nondestructive evaluation of reinforcement bars using ground-penetrating radar and electromagnetic induction data," *Comput.-Aided Civil Infrastruct. Eng.*, vol. 37, no. 14, pp. 1834–1853, Nov. 2022.

[55] R. Yurt, H. Torpi, P. Mahouti, A. Kizilay, and S. Koziel, "Buried object characterization using ground penetrating radar assisted by data-driven surrogate-models," *IEEE Access*, vol. 11, pp. 13309–13323, 2023.

[56] Q. Dai, Y. H. Lee, H.-H. Sun, G. Ow, M. L. M. Yusof, and A. C. Yucel, "3DInvNet: A deep learning-based 3D ground-penetrating radar data inversion," *IEEE Trans. Geosci. Remote Sens.*, vol. 61, 2023, Art. no. 5105016, doi: 10.1109/TGRS.2023.3275306.

[57] O. Patsia, A. Giannopoulos, and I. Giannakis, "A deep learning framework for ground penetrating radar," in *Proc. 11th Int. Workshop Adv. Ground Penetrating Radar (IWAGPR)*, Valletta, Malta, Dec. 2021, pp. 1–6.

[58] J. Wang et al., "Deep learning-based rebar clutters removal and defect echoes enhancement in GPR images," *IEEE Access*, vol. 9, pp. 87207–87218, 2021.

[59] E. Temlioglu and I. Erer, "A novel convolutional autoencoder-based clutter removal method for buried threat detection in ground-penetrating radar," *IEEE Trans. Geosci. Remote Sens.*, vol. 60, 2022, Art. no. 5103313.

[60] H.-H. Sun, W. Cheng, and Z. Fan, "Learning to remove clutter in real-world GPR images using hybrid data," *IEEE Trans. Geosci. Remote Sens.*, vol. 60, 2022, Art. no. 5113714.

[61] A. Liseno and R. Pierri, "Imaging perfectly conducting objects as support of induced currents: Kirchhoff approximation and frequency diversity," *J. Opt. Soc. Amer. A, Opt. Image Sci.*, vol. 19, no. 7, pp. 1308–1343, Jul. 2002.

[62] R. Pierri, R. Solimene, A. Liseno, and J. Romano, "Linear distribution imaging of thin metallic cylinders under mutual scattering," *IEEE Trans. Antennas Propag.*, vol. 53, no. 9, pp. 3019–3029, Sep. 2005.
[63] R. Solimene, A. Brancaccio, J. Romano, and R. Pierri, "Localizing thin metallic cylinders by a 2.5-D linear distributional approach: Experimental results," *IEEE Trans. Antennas Propag.*, vol. 56, no. 8, pp. 2630–2637, Aug. 2008.
[64] M. Bertero and P. Boccacci, *Introduction to Inverse Problems in Imaging*. Boca Raton, FL, USA: CRC Press, 1998.
[65] N. Srivastava, G. Hinton, A. Krizhevsky, I. Sutskever, and R. Salakhutdinov, "Dropout: A simple way to prevent neural networks from overfitting," *J. Mach. Learn. Res.*, vol. 15, no. 56, pp. 1929–1958, 2014.
[66] K. He, X. Zhang, S. Ren, and J. Sun, "Deep residual learning for image recognition," in *Proc. IEEE Conf. Comput. Vis. Pattern Recognit. (CVPR)*, Jun. 2016, pp. 770–778.
[67] C. Warren, A. Giannopoulos, and I. Giannakis, "GprMax: Open source software to simulate electromagnetic wave propagation for ground penetrating radar," *Comput. Phys. Commun.*, vol. 209, pp. 163–170, Dec. 2016.
[68] I. Catapano, A. Affinito, G. Gennarelli, F. di Maio, A. Loperte, and F. Soldovieri, "Full three-dimensional imaging via ground penetrating radar: Assessment in controlled conditions and on field for archaeological prospecting," *Appl. Phys. A, Solids Surf.*, vol. 115, no. 4, pp. 1415–1422, Jun. 2014.

Giuseppe Esposito received the M.Sc. degree (summa cum laude) in aerospace engineering and the Ph.D. degree in industrial engineering from the University of Naples Federico II, Naples, Italy, in 2018 and 2023, respectively.

Since 2019, he has been collaborating with the Institute for Electromagnetic Sensing of the Environment (IREA), National Research Council of Italy (CNR), Naples. From May 2022 to July 2022, he was a Visiting Researcher with the University of Illinois at Chicago (UIC), Chicago, IL, USA. His research interests include the field of unmanned aerial vehicle-based radar imaging, with emphasis on platform positioning, data synchronization, sensor fusion, and inverse scattering approaches.

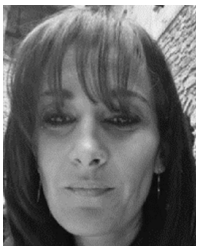

Ilaria Catapano (Member, IEEE) received the Ph.D. degree in electrical and information engineering from the University of Cassino, Cassino, Italy, in 2006.

In 2003, she started her research activity at the Institute for Electromagnetic Sensing of the Environment (IREA), National Research Council of Italy (CNR), Naples, Italy. She is currently a Research Scientist with CNR, level II. Her skills are about electromagnetic modeling, forward and inverse scattering problems, remote and in situ microwaves, and TeraHertz (THz) sensing techniques. She was an Adjunct Professor with Mediterranea University, Reggio Calabria, Italy, in 2010; and an Invited Lecturer with São Paulo University, São Paulo, Brazil, in 2013, and the Indian Institute of Technology Kharagpur, Kharagpur, India, in 2016. She has published more than 170 published articles with over 90 international journal articles. Her research interests include radar imaging with a focus on processing of experimental data gathered by means of ground-based, airborne, and drone radar systems, THz spectroscopy and imaging, measurement campaigns carried out by means of microwave and THz devices, development of high-frequency radar systems and data processing strategies for target detection and tracking and vital signs monitoring, and use of microwaves and THz for food inspections and medical imaging.

Dr. Catapano received the Giorgio Barzilai Award by the Italian Electromagnetic Society (SIEM) in 2004 and was one of the young scientist awardees at the XXIX URSI General Assembly in 2008. She is an Associate Editor of IEEE TRANSACTIONS ON COMPUTATIONAL IMAGING and a referee for many international journals.

Giovanni Ludeno received the M.S. degree in telecommunication engineering from the University "Mediterranea" of Reggio Calabria, Reggio Calabria, Italy, in 2011, and the Ph.D. degree in electronics and computer engineering from the University of Campania "Luigi Vanvitelli," Caserta, Italy, in 2015.

From November 2011 to October 2012, he was a Scholar with the Institute for Electromagnetic Sensing of the Environment (IREA), National Research Council of Italy (CNR), Naples, Italy, where he has been a Research Scientist since 2015. From October 2012 to January 2014, he was a Research Fellow with Vitrociset SpA, Rome, Italy. He has coauthored over 60 publications in international peer-reviewed journals, conference proceedings, and books. His research interests include the field of applied electromagnetism, with special regard to remote and in situ sensing.

Dr. Ludeno was a Guest Editor for a special issue in *Journal of Marine Science of Engineering* (MDPI) of which now he is a Topic Editor.

Francesco Soldovieri is currently the Research Director of the Institute for Electromagnetic Sensing of the Environment (IREA), National Research Council of Italy (CNR), Naples, Italy. He is the coauthor of over 240 papers on national and international journals and more than 350 conference proceedings. His research interests include radar imaging, data processing for GPR, indoor surveillance, through-wall imaging, passive radars, integration of geophysical data, and radars for planetary exploration.

Mr. Soldovieri was the General Chair of the International Workshop on Advanced Ground Penetrating Radar 2007 and the General Co-Chair of the Ground Penetrating Radar Conference 2010. He was a member of the Editorial Board of IEEE GEOSCIENCE AND REMOTE SENSING LETTERS and is a member of IEEE TRANSACTIONS ON COMPUTATIONAL IMAGING, IEEE TRANSACTIONS ON GEOSCIENCE AND REMOTE SENSING, and *Remote Sensing* (MDPI). He is the Editor-in-Chief of *Heritage*, a MDPI journal devoted to Cultural and Natural Heritage. He has been a Scientific Coordinator of the FP7 projects ISTIMES and AMISS and a Technical Manager of the H2020 Project HERACLES. He has been the President of the Division on Geosciences Instrumentation and Data Systems of European Geosciences Union.

Gianluca Gennarelli received the M.Sc. degree (summa cum laude) in electronic engineering and the Ph.D. degree in information engineering from the University of Salerno, Salerno, Italy, in 2006 and 2010, respectively.

From 2010 to 2011, he was a Post-Doctoral Fellow with the University of Salerno. Since 2012, he has been a Research Scientist with the Institute for Electromagnetic Sensing of the Environment (IREA), National Research Council of Italy (CNR), Naples, Italy. In 2015, he was a Visiting Scientist with the NATO-CMRE, La Spezia, Italy. He has coauthored over 100 publications in international peer-reviewed journals and conference proceedings. His research interests include microwave sensors, antennas, inverse scattering problems, radar imaging and signal processing, diffraction problems, and electromagnetic simulation.

Dr. Gennarelli serves as a reviewer for several international journals and conference papers.

Open Access funding provided by 'Consiglio Nazionale delle Ricerche-CARI-CARE-ITALY'
within the CRUI CARE Agreement